NSRR C-J04659 (2015)

JSS Focus Issue on Advanced Interconnects: Materials, Processing, and Reliability

Effect of Porogen Incorporation on Pore Morphology of Low-k SiC_xN_y Films Prepared Using PECVD

Hung-En Tu,[a] Chun-Jen Su,[b] U-Ser Jeng,[b] and Jihperng Leu[a,z]

[a]Department of Materials Science and Engineering, National Chiao Tung University, Hsinchu 30010, Taiwan
[b]National Synchrotron Radiation Research Center, Hsinchu Science Park, Hsinchu 30076, Taiwan

Low-k porous SiC_xN_y films were prepared through plasma-enhanced chemical vapor deposition, using 1,3,5-trimethyl-1,3,5-trivinylcyclotrisilazane (VSZ) as the matrix precursor and epoxycyclohexane (ECH) as a porogen. The effects of porogen loading and deposition temperature on porogen incorporation, pore morphology, and the properties of porous SiC_xN_y films were examined. In addition, the impact of film shrinkage and the corresponding nanopore structures after annealing were studied. The porosity of films deposited at 100°C increased from 1.8% to 19.8% when ECH loading increased to 30%, above which the porosity remained nearly constant because of high film shrinkage. The pore size decreased slightly from 4.1 to 3.7 nm when ECH loading increased to 30%, above which the pores became larger and were broadly distributed. By contrast, increasing deposition temperature at 20% ECH loading decreased porogen incorporation and increased film density. The porosities and pore size of films decreased, respectively, when the deposition temperature increased. A short-range ordering of pores was observed only at low deposition temperatures because the N-Si-C cross-linked structures and organic phase were present. Optimized processing parameters facilitated the fabrication of low-k porous SiC_xN_y films exhibiting 19.8% porosity, 3.7-nm pores, a k value of 3.18, and an elastic modulus of 7.7 GPa.
© The Author(s) 2014. Published by ECS. This is an open access article distributed under the terms of the Creative Commons Attribution 4.0 License (CC BY, http://creativecommons.org/licenses/by/4.0/), which permits unrestricted reuse of the work in any medium, provided the original work is properly cited. [DOI: 10.1149/2.0031501jss] All rights reserved.

Manuscript submitted July 18, 2014; revised manuscript received September 22, 2014. Published October 2, 2014. *This paper is part of the JSS Focus Issue on Advanced Interconnects: Materials, Processing, and Reliability.*

In CMOS backend interconnections, low-k etch-stop/dielectric barrier materials such as silicon carbonitride (SiC_xN_y) (k = 4.5–5.5) and ultralow-dielectric-constant (ultralow-k, ULK) inter-layer dielectrics (ILDs) have been used to lower the effective capacitance (k_{eff}) in the 45 and 32 nm node and beyond.[1] Silicon carbonitride films are typically prepared by performing plasma-enhanced chemical vapor deposition (PECVD) of multi-precursors such as silane/ammonia (or nitrogen)/methane[2,3] and trimethylsilane/amonia.[4] Recently, single source precursors such as hexamethyldisilazane[5] and BASICN[6] have been used for preparing dense low-k SiC_xN_y films by using PECVD because these films display low defects (i.e., low leakage current) and higher etch selectivity due to high C/Si ratio.[6] To further reduce the dielectric constant of silicon carbonitride film, incorporation of porosity is one of the primary approaches, in addition to continued addition of elements with lower polarizability such as more C atoms.

A conservative approach was proposed by Nguyen et al.,[7] who prepared a dielectric barrier bilayer of dense SiN_y/porous SiC_xN_y, exhibiting 12% porosity, by performing plasma deposition of dimethylsilacyclopentane and NH_3 and then using UV to cure the samples. The dense films of the bilayer on top helped protect the underlying copper layer against plasma-induced damage and oxidation caused by the diffusion of oxygen, whereas the bottom porous film of the bilayer contributed to a reduction in the dielectric constant.[8] Because they possess a bilayer (dense film/porous film) or sandwich (dense film/porous film/dense film) structure, porous low-k SiC_xN_y films can serve as the etch stop/dielectric barrier layer with a lower effective k. Opportunely, recent introduction of selective metal-capping materials such as CoW(P)[9] to passivate copper lines may relax the etch-stop layer diffusion-barrier requirements and allow the k-value of the etch-stop layer, without using sandwich structure, to be scaled aggressively to advance the k_{eff} scaling, for example, by incorporating porosity.[10]

1,3,5-trimethyl-1,3,5-trivinylcyclotrisilazane (VSZ), a cyclic organosilazane with 3 vinyl side-groups as illustrated in Fig. 1a, has been used as the single source precursor for depositing low-k SiC_xN_y by using PECVD and a low power density (0.15 W/cm^3) to obtain SiC_xN_y films of low dielectric constant ranging between 3.6 and 4.6 for deposition temperatures ranging from 25 to 400°C.[11] These as-deposited films also possess low film density of 1.6–2.0 g/cm^3, which can be attributed to the existence of micropores, but limited porosity, in the as-deposited SiC_xN_y films due to the induced pores resulting from organic phase and the formation of Si-$(CH_2)_n$-Si with the matrix structure.[12]

In order to explore and fabricate porous SiC_xN_y films with higher porosity, a sacrificial porogen, epoxycyclohexane (ECH) as illustrated in Fig. 1b, was added to the feed stream of the VSZ precursor in this study. A SiC_xN_y/porogen hybrid film was first deposited at various temperatures (100 to 300°C), and the porogen was then removed by heating at 400°C to generate low-k porous SiC_xN_y films. When reducing the k value of the etch-stop/barrier film and fabricating devices, understanding how to control the porosity and pore size in porous low-k SiC_xN_y films is critical. Thus, the pore morphology (size and distribution), density, and structure of as-deposited SiC_xN_y/porogen hybrid films and post-annealed porous SiC_xN_y films were examined using GISAXS, X-ray reflectivity (XRR), and FTIR analyses. Furthermore, the effects of porogen ratio in the gas feed and deposition temperatures on the pore morphology and the mechanical and dielectric properties of porous SiC_xN_y films were determined.

Experimental

PECVD was used to deposit SiC_xN_y or hybrid SiC_xN_y/porogen films onto silicon wafers; a liquid monomer, VSZ (Gelest, Inc. 95%), was used as the matrix precursor in the presence and absence of ECH (Alfa Aesar, 98%+), the porogen precursor. The deposition was performed in a radio-frequency (RF) (13.56 MHz) parallel-plate PECVD system. The two liquid precursors were vaporized at 60°C to prevent condensation in the pipe and were carried into the reactor by an Ar carrier gas. The deposition pressure and RF power were maintained at 90 mTorr and 50 W (power density = 0.15 W/cm^3), respectively, without bias. The deposition temperatures were from 100°C to 300°C. Moreover, the effect of 10%–50% porogen loading in the gas feed (total flow rate, 20 sccm) on the incorporation of porosity and pore morphology was examined; the porogen loading in the gas feed was defined as the ratio of the porogen flow rate to the sum of the matrix and porogen flow rates. Subsequently, the annealing step

[z]E-mail: jimleu@mail.nctu.edu.tw

Downloaded on 2015-03-15 to IP 60.251.210.233 address. Redistribution subject to ECS terms of use (see ecsdl.org/site/terms_use) unless CC License in place (see abstract).

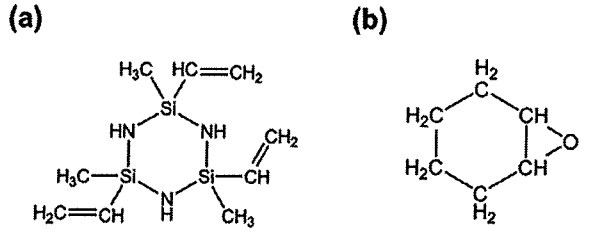

Figure 1. Original structures of (a) matrix precursor, VSZ and (b) porogen precursor, ECH.

was performed at 400°C for 3 h in an Ar atmosphere to incinerate and eliminate the sacrificial porogen present in the as-deposited hybrid SiC_xN_y/porogen films and thus generate the porous SiC_xN_y films.

Chemical bonding in the hybrid SiC_xN_y/porogen and porous SiC_xN_y films was examined using FTIR spectroscopy (MAGNA-IR Technology Protege 460) at a normal incident angle under the transmission mode. The FTIR spectra were collected (using a total of 32 scans) in the 500–4000 cm^{-1} range, at a resolution of 4 cm^{-1}.

Pore morphology was characterized using a BL23A GISAXS instrument at the National Synchrotron Radiation Research Center, Taiwan. All 2D GISAXS patterns were recorded using an area detector at a fixed incident angle of 0.2° of the 10-keV X-ray beam (diameter, 0.5 mm). Pore size was extracted from the GISAXS data by using the Guinier approximation.[13] The porosity of the porous SiC_xN_y films was deduced from the film density that was determined using an XRR instrument (Bruker D8 Discover) equipped with a Cu K_α source (λ = 0.154 nm). The XRR data were analyzed using LEPTOS simulation software. Film porosity P of the porous SiC_xN_y films was calculated using Eq. 1:[14,15]

$$\rho = \rho_o(1 - P) \quad [1]$$

where ρ and ρ_o are the densities of the porous SiC_xN_y films and PECVD VSZ-matrix films that were determined using the XRR data, respectively.

The dielectric constant (k) of the porous SiC_xN_y films was calculated from the capacitance-voltage (C-V) (HP 4280) measurement obtained using the metal-insulator-semiconductor (MIS) structural configuration [Al electrode/SiC_xN_y film/Si (10 ohm-cm)] at room temperature. To accurately measure the dielectric constant by using the C–V dot measurement, three circular aluminum dots of nominal diameters were used (to minimize the geometric effect). Aluminum electrodes (1 μm thick) were coated onto the dielectric films by using a ULVAC EBX-6D thermal evaporator through a shadow mask. For the C-V measurements, the thickness of the SiC_xN_y films was approximately 100 nm; film thickness was measured using an n&k Analyzer 1280 (n&k Technology, Inc.).

Nanoindentation tests were performed with a nanoindentor (MTS Nano Indenter XP System) equipped with a Berkovich tip, in continuous mode, to obtain the reduced modulus (E_r). The Oliver–Pharr method[16] was then used to determine the elastic modulus (E) of various SiC_xN_y films. To eliminate the effect of the Si substrate, the indentation depth was maintained at <20% of the film thickness (nominal thickness: 1 μm).

Results and Discussion

Pore morphology of SiC_xN_y/porogen hybrid films and porous SiC_xN_y films prepared using various ECH porogen loadings.— ECH was added as a porogen to the VSZ precursor feed gas to prepare SiC_xN_y/porogen hybrid films and investigate how ECH can be used to control pore size and porosity and the dielectric constant of porous SiC_xN_y films after removing the porogen. Hybrid SiC_xN_y/porogen films were deposited at 100°C, using various ECH loadings relative to the VSZ matrix precursor. First, the porogen sizes of these hybrid films were characterized using GISAXS. The 2D scattering patterns of the SiC_xN_y/porogen hybrid films as a function of porogen loading are presented in Fig. 2a, and the corresponding GISAXS profiles in the in-plane and out-of-plane scattering directions are plotted in Figs. 3a and 3b. When the porogen loading was ≤ 20%, the scattering patterns exhibited rod-like scattering peaks along the in-plane direction (indicated by the arrow in Fig. 2a), implying an in-plane ordered porogen structure. Based on the peak position q_p, the mean spacing between porogens was calculated using the Bragg law, $L = 2\pi/q_p$, revealing a decrease from 61.5 to 53.6 nm with an increase in porogen loading (Table I). A porogen loading of > 20%, the scattering patterns exhibited no ordered distribution of the porogen. The Guinier plots (ln I vs. q_z^2) drawn for SiC_xN_y/porogen hybrid films prepared using various ECH loadings are presented in Fig. 3c. All the GISAXS data in the q-range with $qR_g \leq 1.0$ were fitted using Guinier approximation,[17] and from the slopes of the fitted Guinier approximation, $-R_g^2/3$ in (Fig. 3c), the radii of gyration R_g were determined for the various porogen sizes in the SiC_xN_y/porogen hybrid films. Moreover, assuming spherical pores, the porogen/pore size was determined as $D = 2(5/3)^{0.5}R_g$.[17] Thus, the porogen sizes were determined to be between 5.4 ± 0.5 nm and 6.2 ± 0.6 nm, depending on porogen loading and the existence of a porogen correlation distance (Table I); the data for 0% porogen were obtained from the accompanying article.[12]

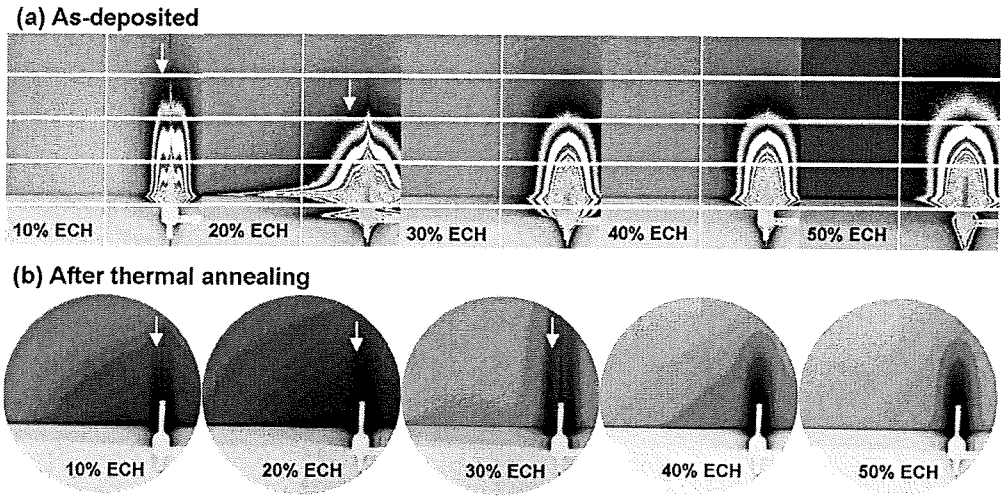

Figure 2. 2D GISAXS scattering patterns of the SiC_xN_y films as a function of porogen loading (a) as-deposited SiC_xN_y/porogen hybrid films at 100°C and (b) porous SiC_xN_y films after thermal annealing at 400°C for 3 h.

Downloaded on 2015-03-15 to IP 60.251.210.233 address. Redistribution subject to ECS terms of use (see ecsdl.org/site/terms_use) unless CC License in place (see abstract).

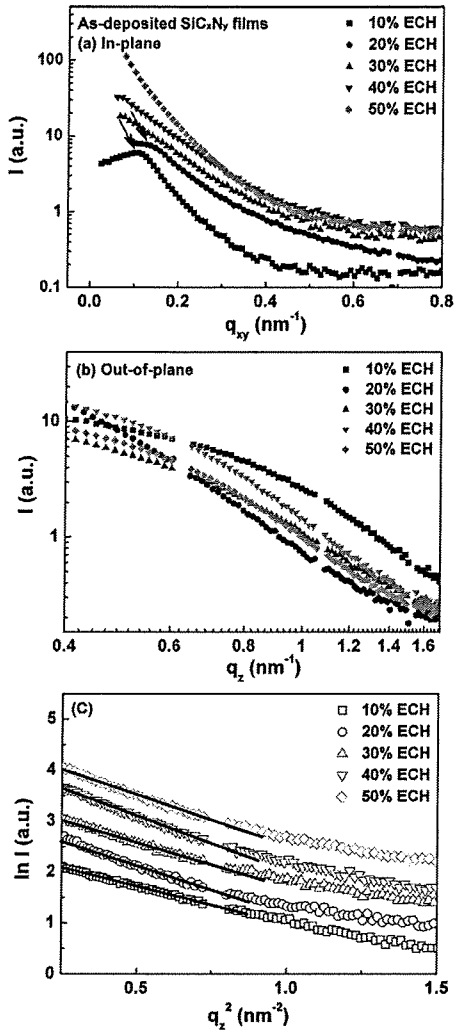

Figure 3. GISAXS scattering profiles of the as-deposited SiC_xN_y/porogen hybrid films at 100°C with different porogen loadings: (a) in-plane, (b) out-of-plane scattering direction, and (c) Guinier plots (ln I vs. q_z^2) from the out-of-plane scattering profiles. The solid lines were obtained by fitting the data using the Guinier approximation.

After the removal of the porogen by heating the film at 400°C for 3 h, which was validated using FTIR analysis porous low-k SiC_xN_y films were formed efficiently, which was demonstrated using GISAXS: Fig. 2b presents the 2D scattering patterns of the porous SiC_xN_y films as a function of porogen loading. The scattering patterns are asymmetric at ECH loading $\leq$ 30%, revealing rod-like in-plane ordered peaks derived from an orderly distribution of pores. However, the mean size and spacing of the pores differed from those of the pores in hybrid SiC_xN_y/porogen films prepared using $\leq$ 20% ECH loadings, which could be due to the higher density contrast between the pore and SiC_xN_y matrices. Figures 4a and 4b illustrate the in-plane and out-of-plane scattering profiles of porous SiC_xN_y films, which were extracted from the data presented in Fig. 2b. The peak position of maximal intensities in the in-plane scattering profiles indicates an ordered distribution of the pores. Moreover, the deduced mean spacing of the pores decreased from 68.2 to 41.7 nm when the porogen loading was increased from 10% to 30%, implying a drastic increase in pores density. However, at 40% and 50% porogen loadings, the loss of the ordered-spacing peaks in the GISAXS patterns suggests that the pores were randomly distributed, presumably because of the presence of excessive numbers of porogens.

The Guinier plots (ln I vs. q_z^2) drawn for porous SiC_xN_y films prepared using various ECH loadings are presented in Fig. 4c. Based on the slopes of the fitted Guinier approximation in the range $qR_g \leq 1.0$,[17] the average pore size (3.7–3.9 nm) of porous SiC_xN_y films was determined to remain near constant when porogen loading was continuously increased, up to 30%, after which the mean spacing between pores decreased substantially with an increase in loading, from 68.2 to 41.7 nm (Fig. 4d), implying a drastic increase in the number of the pores of constant size. Above loadings of 40% and 50% (Fig. 4d and Table I), the pore size increased considerably, to approximately 5 nm, and exhibited a broadened size distribution; this was accompanied by a loss of the mean pore spacing, which resulted in a random distribution of the pores.[18] These results indicate that a marked increase in pore number led to an enlargement of pores, which occurred because the pores aggregated when the porogen loading was increased to 40% and 50%.

FTIR analysis of SiC_xN_y/porogen hybrid and porous SiC_xN_y films.— The chemical bonding and structures of SiC_xN_y/porogen hybrid films were next examined using FTIR spectroscopy. Figure 5a presents the FTIR spectra of liquid ECH and the PECVD-ECH film. In liquid ECH, the characteristic CH_2- and CH- absorption bands represent the symmetric stretching vibration of the CH_2 bond at 2860 cm^{-1}, the asymmetric stretching vibration of the CH_2 bond at 2940 cm^{-1}, and the C-H epoxy bond at 2990 cm^{-1}. By comparison, in the spectrum of the PECVD-ECH film, the absorption band at 2990 cm^{-1} (C-H epoxy) is absent, but the symmetric and asymmetric stretching vibrations of the CH_2 bond are retained at 2879 and 2933 cm^{-1}, respectively,[19–21] with the bands being slightly broader. However, several new absorption bands appeared in the spectrum, including one at 1660 cm^{-1}, representing the carbonyl C = O group in a cyclic ketone,[22,23] and a broad absorption band at approximately 3400 cm^{-1}, which corresponding to the stretching vibration of the O-H bond. These absorption bands indicate that upon plasma deposition, chain scission of the ether bond (C-O) in epoxide[24] occurred readily and generated a ketone group and possibly hydroxyl groups, with a trace of H_2O produced in the chamber or upon exposure to ambient air,[25] whereas the majority of the cyclohexane ring was retained. Thus, the CH_2 stretching bands and the C = O absorption band were used to monitor the amount of porogen incorporated in the

Table I. Porogen/Pore size, porogen/pore correlation, porosity and film shrinkage of as-deposited SiC_xN_y/porogen hybrid films at 100°C under various porogen loading and their corresponding porous SiC_xN_y films after thermal annealing at 400°C.

	As-deposited SiC_xN_y/ porogen hybrid film		Porous SiC_xN_y film after thermal annealing					
Porogen loading	D (nm)	L (nm)	D (nm)	L (nm)	Porosity (%)	Film shrinkage (%)	Modulus (GPa)	k
0% ECH	4.9 ± 0.4	30.1	4.1 ± 0.4	29.5	-	1.3	20.2	3.64
10% ECH	5.4 ± 0.5	61.5	3.9 ± 0.2	68.2	1.8	3.9	10.5	3.52
20% ECH	6.1 ± 0.7	53.6	3.8 ± 0.2	68.2	12.3	4.3	8.7	3.27
30% ECH	6.0 ± 0.6	-	3.7 ± 0.4	41.7	19.8	15.9	7.7	3.18
40% ECH	6.2 ± 0.6	-	5.1 ± 0.5	-	20.0	16.8	6.2	3.12
50% ECH	6.1 ± 0.6	-	5.3 ± 0.6	-	20.2	19.7	5.9	3.15

Downloaded on 2015-03-15 to IP 60.251.210.233 address. Redistribution subject to ECS terms of use (see ecsdl.org/site/terms_use) unless CC License in place (see abstract).

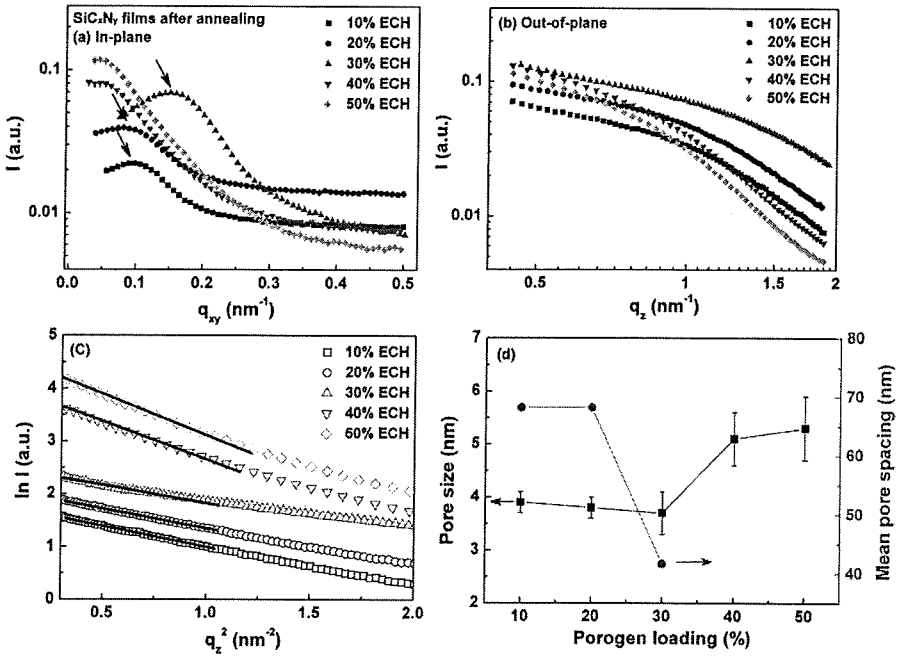

Figure 4. GISAXS scattering profiles of the porous SiC_xN_y films with different porogen loading after annealing at 400°C for 3 h: (a) in-plane, (b) out-of-plane scattering direction, (c) Guinier plots ($\ln I$ vs. q_z^2) from the out-of-plane scattering profiles, and (d) pore size and mean pore spacing as a function of porogen loading. The solid lines were obtained by fitting the data using the Guinier approximation.

SiC_xN_y/porogen hybrid films during film deposition and the decomposition of the porogen when the porous SiC_xN_y films were generated upon thermal annealing at 400°C.

Fig. 5b presents the FTIR spectra of the SiC_xN_y/porogen hybrid films prepared by performing PECVD and using various ECH porogen loadings; these can be compared with the spectrum of the PECVD-ECH film shown at the bottom of the figure. All spectra of the hybrid films were normalized to the main matrix structure, the Si-N-Si peak at approximately 1047 cm^{-1}. The characteristic features of the hybrid films were similar to those observed in the pure VSZ films prepared using PECVD at a deposition temperature of 100°C, which is described in the accompanying article.[11] The main bondings in the hybrid films included the asymmetric stretching vibration of Si-N bonds at 922 and 1047 cm^{-1},[26] the bending vibration of the $Si-CH_3$ bonds at 1265 cm^{-1}, the bending vibration of the C-H in $Si-CH_2-Si$ bonds at 1375 cm^{-1}, the wagging vibration of C-H in CH_2 at 1460 cm^{-1},[20,24] the asymmetric and symmetric stretching vibration of $C-H_x$ bonds at 2800–3010 cm^{-1},[21,24] and the bending and stretching vibration of N-H bonds at 1150 and 3370 cm^{-1}.[27] When ECH porogen was added to the hybrid films, the Si-N absorption band was shifted to a higher wavenumber, to 1080 cm^{-1} from 1047 cm^{-1} (0% porogen), as shown in the inset in Fig. 4b. The blueshift possibly occurred because of an increase in the Si-N-Si bond angle caused by the inclusion of the porogen phase.[28]

With increasing ECH porogen loading, the intensities of the CH_2 and C = O absorption bands of the porogen in the hybrid films, representing the amounts of incorporated porogen, increased clearly. The amounts of porogen incorporated in the films at distinct porogen loadings were estimated based on the ratio of the peak areas of CH_x bonds (2800–3100 cm^{-1}) relative to 0% porogen (Fig. 6). The amount of porogen incorporated increased linearly, up to 30%, after which the amount increased at a higher rate. Thus, the porogen was incorporated

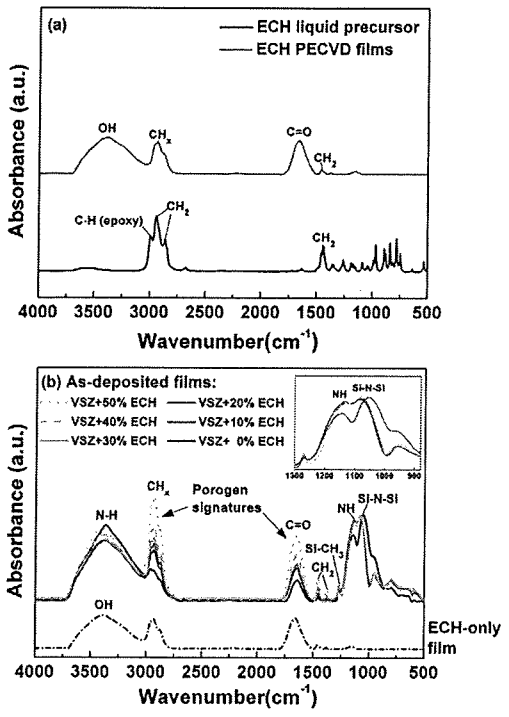

Figure 5. FTIR spectra of (a) liquid ECH and PECVD ECH and (b) as-deposited PECVD SiC_xN_y/porogen hybrid films at 100°C using VSZ and various ECH porogen loadings.

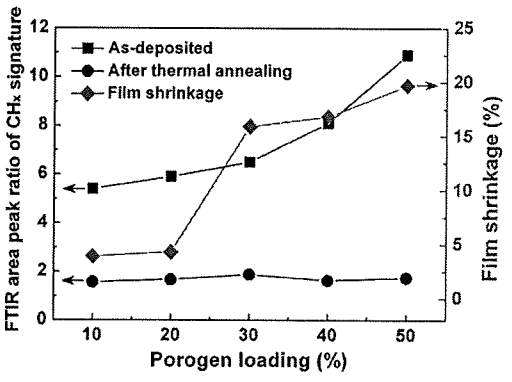

Figure 6. FTIR area peak ratio of CH_x bond for as-deposited SiC_xN_y/porogen hybrid films, porous SiC_xN_y films and their film shrinkage after annealing at 400°C for 3h, as a function of porogen loading.

Downloaded on 2015-03-15 to IP 60.251.210.233 address. Redistribution subject to ECS terms of use (see ecsdl.org/site/terms_use) unless CC License in place (see abstract).

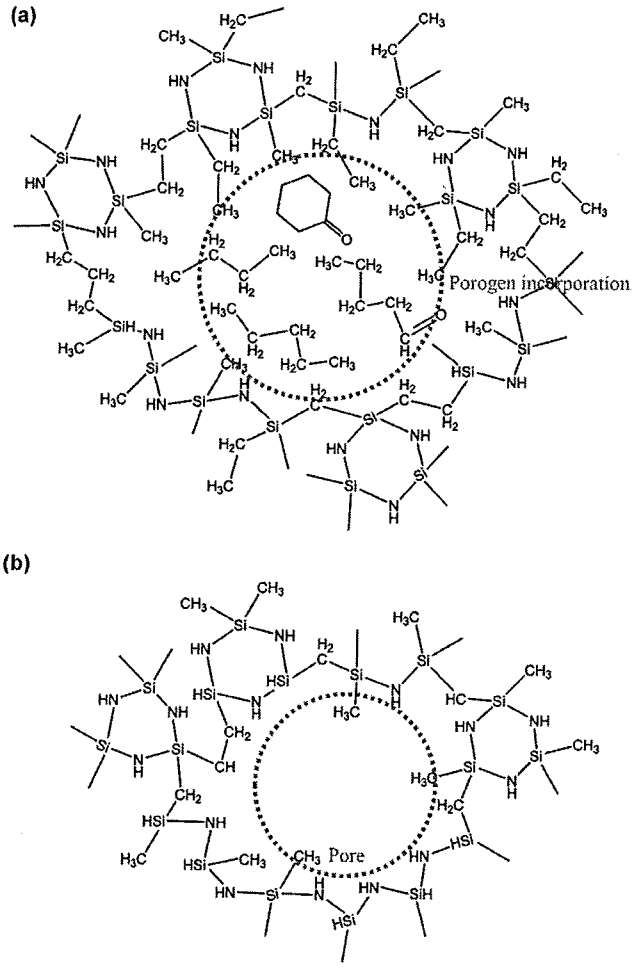

Figure 7. Schematic of structure model for (a) SiC_xN_y/porogen hybrid films, and (b) porous SiC_xN_y films.

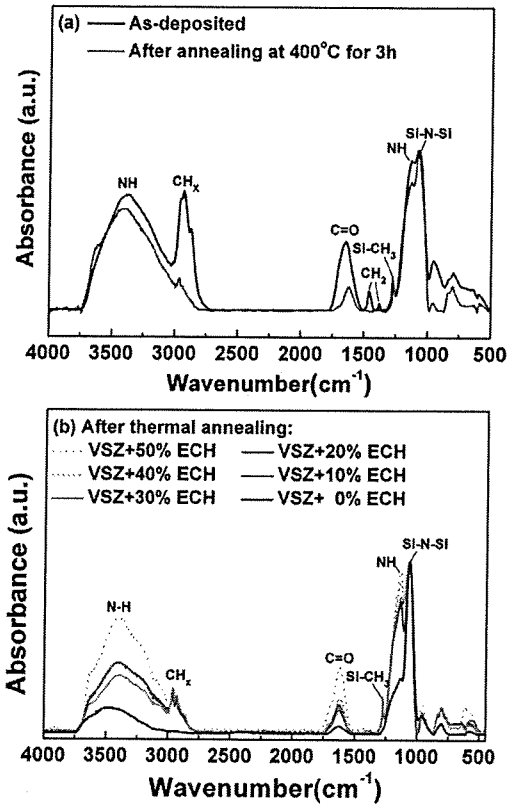

Figure 8. FTIR spectra of (a) as-deposited SiC_xN_y/porogen hybrid film and post-annealed porous SiC_xN_y using 20% ECH porogen loading, and (b) porous SiC_xN_y films prepared using various ECH porogen loadings, after annealing at 400 °C for 3 h.

and it filled the loose voids in the SiC_xN_y matrix as schematically illustrated in Fig. 7a, because no variation in film structures was detected after adding the porogen. The detailed description of the SiC_xN_y film prepared by VSZ only can be found elsewhere.[12] When a small amount of porogen (<30% ECH loadings) was incorporated into the film, the porogens slightly increased the pore correlation distance (as listed in Table I), but did not disrupt the short-range ordered arrangement of pores. At ≥ 30% ECH loadings, the increase in porogen incorporation resulted in an enhanced randomness in porogen distribution in the films.

After preparing the films, an annealing step (400°C for 3 h) was used to remove the porogen incorporated in the SiC_xN_y/porogen hybrid films and generate porous SiC_xN_y films as schematically shown in Fig. 7b. Figure 8a presents the FTIR spectra of the as-deposited SiC_xN_y/porogen hybrid film at 20% ECH loading and its corresponding porous SiC_xN_y film formed after thermal annealing. The intensities of the characteristic absorption peaks of the porogen (at 1660 and 2800–3010 cm^{-1}) decreased substantially, indicating that the sacrificial porogen was effectively incinerated and eliminated and that the porous SiC_xN_y film was formed. However, the Si-CH_3 absorption band (1265 cm^{-1}) was retained in the film after thermal annealing. Fig. 8b presents the FTIR spectra of porous SiC_xN_y films that were prepared using various porogen loadings and then annealed at 400°C for 3 h. The intensities of the characteristic absorption peaks of the porogen decreased when porogen loading was increased from 10% to 50%. Specifically, the CH_x component (at 2800–3010 cm^{-1}) remained low and almost constant at 10%–50% porogen loadings, which is illustrated by the CH_x peak ratio plot in Fig. 6. This is distinct from the change observed in the pure SiC_xN_y film (0% porogen), in which -CH_3 disappeared completely after thermal annealing, as indicated by the presence of Si-CH_3 absorption (1265 cm^{-1}) and CH_x stretching bands (2800–3010 cm^{-1}). These results indicate that annealing effectively incinerated and removed the incorporated porogen, but that the pendent Si-CH_3 of the VSZ matrix remained intact. Moreover, the main Si-N absorption band was shifted from 1080 cm^{-1} (0% ECH) to a lower wavenumber (1068 cm^{-1}; 20% ECH) after the decomposition of the porogen upon thermal annealing. The redshift indicates that when the porogen was removed, the film shrank (Fig. 6) and led to a reduction in the Si-N-Si bonding angle.[29,30]

In addition to analyzing film structure and measuring pore sizes, the porosity of the porous SiC_xN_y films generated after thermal annealing was quantified using XRR. Table I summarizes the pore morphology, porosity, and shrinkage results collected for the porous SiC_xN_y films. The porosities of porous SiC_xN_y films increased from 1.8% to 19.8% when the porogen loading was increased from 10% to 30%. Above 30% porogen loading, the porosity peaked at approximately 20.0%, which is distinct from the trend of porogen incorporation determined using FTIR analysis (Fig. 6). The constant porosity at ≥30% ECH loading can be attributed to the shrinking of the film when the porous SiC_xN_y film is formed after the thermal annealing process.[21] The porous SiC_xN_y films shrank by 3.9%–19.7% of the thickness with increasing porogen loading, as shown in Fig. 6 and summarized in Table I. Moreover, porosity did not increase markedly when the film shrank by >15.9%.

By combining the results of pore size and distribution, porosity, structural analysis, and film shrinkage, the effect of porogen loading on the formation of porous SiC_xN_y films can be summarized as follows. At first, SiC_xN_y film without ECH porogen, possessing a pore structure (4.9 nm) and a marginal short-range ordering, was of a low-density

Downloaded on 2015-03-15 to IP 60.251.210.233 address. Redistribution subject to ECS terms of use (see ecsdl.org/site/terms_use) unless CC License in place (see abstract).

and loose structure. Upon adding ECH porogen and plasma deposition processing, a cyclic ketone and smaller fragments such as aliphatic hydrocarbons and their oxygenated species, were incorporated into the voids of the SiC_xN_y matrix generated from pure VSZ precurosr as shown in Fig. 7a. In the as-deposited SiC_xN_y/porogen hybrid films, the porogen size increased slightly, relative to the pore size in the SiC_xN_y film (4.9 nm), prepared using pure VSZ (0% ECH), when the ECH porogen was added at loadings ranging from 10% to 50%. For ECH porogen loading $\leq$10%, the incorporated porogen was too small to fill up the voids of the SiC_xN_y matrix, making no impact on the progen size. However, at porogen loading $\geq$ 20%, the incorporated porogen could fill the voids sufficiently and aggregate to a porogen size of ~6 nm. While the porogen size has remained virtually the same, ~6 nm, above 20% porogen loading, the amount of incorporated porogen still continued to increase as observed by an increase of the porogen signature in FTIR analyses. Moreover, inserting porogens and their smaller fragment might have disrupted pore ordering of the SiC_xN_y matrix containing only VSZ, which was indicated by the increase in mean pore spacing from 30.1 nm at 0% ECH to 61.5 and 53.6 nm at 10% and 20% ECH loading, respectively. GISAXS analysis revealed that at $\geq$ 30% ECH loading, this spatial ordering was not observed in SiC_xN_y/porogen hybrid films because of the large amount of incorporated porogen.

After annealing at 400°C for 3 h, SiC_xN_y films deposited at 100°C, using pure VSZ, exhibited a low level of porosity, a pore size of 4.1 $\pm$ 0.4 nm, and a pore correlation distance of 29.5 nm, which is reported in details elsewhere.[12] The porosity originated mainly from the intrinsic void in the cross-linked structure of the SiC_xN_y films. For SiC_xN_y/porogen hybrid films, the incorporated porogens consisting of cyclic ketone and smaller fragments and some of the organic components such as $-CH_3$ and $-(CH_2)_n-$ attached to SiC_xN_y matrix are thermally decomposed to CH_4, CO_2, H_2O etc., which can readily diffuse out of the film. As a result, a shorter Si–CH_2–Si or Si–$(CH_2)_2$–Si in the skeleton of SiC_xN_y film[12] as well as pore structure are formed as illustrated in Fig. 7b. When porogen loading was 10% and 50%, the porosity increased, reaching 1.8% and 20.2%, respectively. The pore size decreased slightly, from 4.1 to 3.7 nm, when ECH loading was increased from 0% to 30%, presumably because the SiC_xN_y matrix density increased and the film shrank (by up to 15.9%). At porogen loading >30%, large amounts of the porogen were removed, resulting in a random distribution of a large number of pores. Therefore, 30% porogen loading represents a threshold above which the number of pores in the films is considerably high and, consequently, the pore correlation distance is short. The pores became larger and randomly distributed when the ECH loading was increased to 40% and 50%. This can be attributed to the randomness induced by the decomposition of a substantial amount of ECH at the annealing stage: the spatial ordering was disrupted, as indicated by the absence of pore correlation distance, and the pores may exhibit aggregation after ECH decomposition, which was followed by film shrinkage (from 16.8% to 19.7% of the thickness).

Effect of deposition temperature on porous low-k SiC_xN_y films.— The effect of deposition temperature on the morphology of porous SiC_xN_y films was examined next; the films were prepared using 20% ECH porogen, a loading at which film collapse was not detected at 100°C. Fig. 9 presents the FTIR spectra of the SiC_xN_y/porogen hybrid films as a function of deposition temperatures ranging from 100 to 300°C. The intensities of the absorption peaks of C = O bonds at 1660 cm^{-1} and C-H in CH_2 and CH_3 bonds at 1460 and 2800–3010 cm^{-1}, which correspond to ECH porogen structure, decreased with increasing deposition temperature. The Si-N absorption band of the hybrid films shifted from 1080 to 1047 cm^{-1} as a function of deposition temperature (inset in Fig. 9); this redshift indicates that the cyclic N-Si-N structures were disrupted and transformed to a dense Si-N structure. These findings are the same as the results obtained as a function of time for the SiC_xN_y films prepared using the VSZ precursor.[11] Figure 10 presents the ratio of peak areas of the CH_x bonds of the porogen as a function of deposition temperature. The

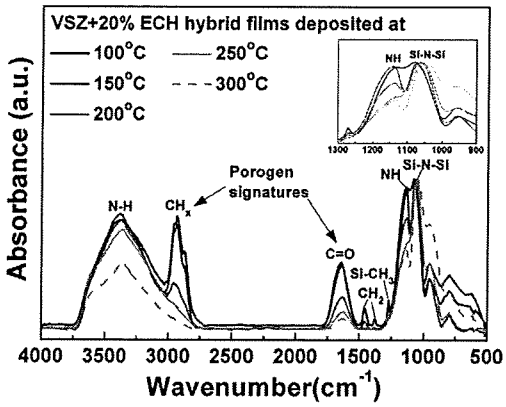

Figure 9. FTIR spectra of as-deposited SiC_xN_y/porogen hybrid films using VSZ + 20% ECH, as a function of deposition temperature.

peak ratio of CH_x bonds in the as-deposited hybrid films decreased with increasing deposition temperature, indicating that less porogen was incorporated when the deposition temperature was elevated. After thermal treatment, all the peak ratios of CH_x bonds were lower than those measured in the absence of thermal treatment.

Figure 11 presents the 2D GISAXS patterns of the SiC_xN_y films as a function of deposition temperature and Fig. 12 presents their corresponding scattering profiles determined for the a) in-plane and b) out-of-plane scattering direction, and c) the Guinier plots (ln I vs. q_z^2) derived from the out-of-plane scattering profiles. Pore morphology (pore size, pore correlation distance, and porosity) of the porous low-k SiC_xN_y films deposited using 20% ECH loading and deposition temperatures ranging from 100 to 300°C was analyzed using the methodology described in previous section and the results are summarized in Table II. With increasing deposition temperature, the pore size decreased from 3.8 $\pm$ 0.2 to 3.0 $\pm$ 0.2 nm and the size distribution of the pores was narrow (Fig. 12d). The pores may have become smaller because porogen incorporation decreased and the density of the film structures increased with an increase in deposition temperature. The pore correlation was lost above a deposition temperature of 250°C. This phenomenon was related to the N-Si-C cross-linked structures of the matrix and Si-$(CH_2)_n$-Si or Si-$(CH_2)_n$-CH_3 of organic chain: at low deposition temperatures, the N-Si-C cross-linked matrix structures and organic phase were present, which resulted in the short-range order in pore distribution; however, when the deposition temperature was increased to 300°C, most of the N-Si-C cross-linked structures and organic chain were eliminated and therefore the pores were

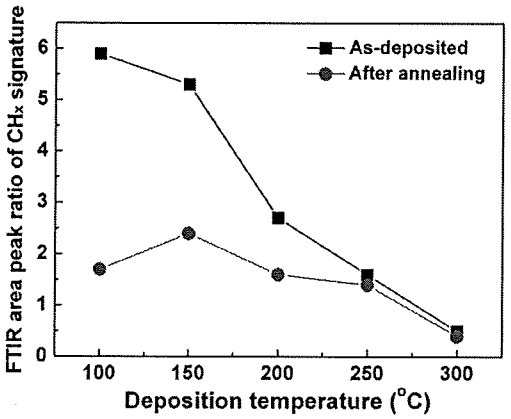

Figure 10. FTIR area peak ratio of CH_x bond for as-deposited SiC_xN_y/porogen hybrid films and porous films as a function of deposition temperature.

Downloaded on 2015-03-15 to IP 60.251.210.233 address. Redistribution subject to ECS terms of use (see ecsdl.org/site/terms_use) unless CC License in place (see abstract).

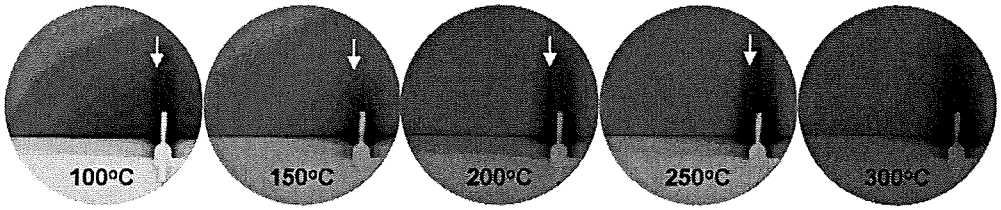

Figure 11. 2D GISAXS scattering patterns of porous SiC_xN_y films, using VSZ + 20% ECH, as a function of deposition temperature.

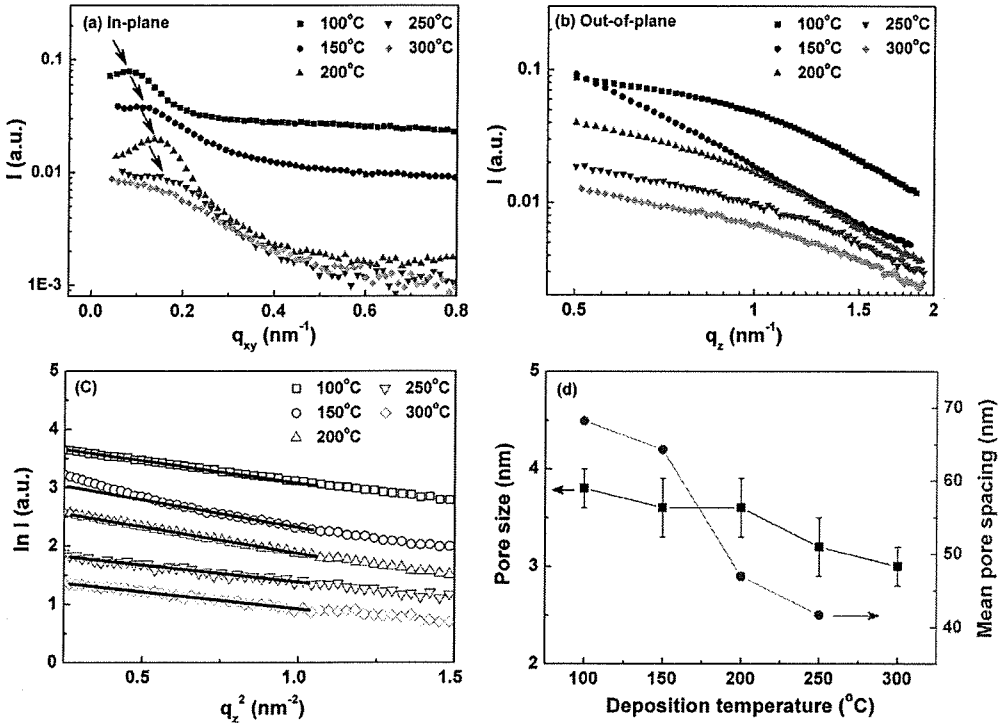

Figure 12. GISAXS scattering profiles of porous SiC_xN_y films, using VSZ + 20% ECH, with different deposition temperature (a) in-plane, (b) out-of-plane scattering direction, (c) Guinier plots (ln I vs. q_z^2) from the out-of-plane scattering profiles, and (d) pore size and mean pore spacing as a function of deposition temperature. The solid lines were obtained by fitting the data using the Guinier approximation.

randomly distributed. The porosity of the porous SiC_xN_y films decreased from 12.3% to 5.3% because of a reduction in the incorporation of the porogen when deposition temperature was increased; this is because porogen incorporation becomes thermodynamically unfavorable at high temperatures. Therefore, when introducing porosity in SiC_xN_y films prepared using the PECVD technique, the level of porogen incorporation is determined by porogen loading and its volatility (and thus deposition temperature), as well as by any shrinkage of the film during thermal decomposition.

Mechanical and dielectric properties of porous SiC_xN_y films.— In this study, porous SiC_xN_y films exhibiting distinct pore morphologies (pore size, distribution, and porosity) were prepared by varying porogen loading and deposition temperature. As shown in Table I, when porogen loading was increased from 0% to 30% at a deposition temperature of 100°C, porosity increased from 1.8% to 19.8%, which led to a reduction in the elastic modulus from 20.2 GPa (0% loading) to 7.7 GPa (30% loading) and in the dielectric constant from 3.64 (0% loading) to 3.18 (30% loading), respectively. At porogen loading $\leq$ 30%, the modulus strength and dielectric constant strongly depended on the porosity, whereas the pore size decreased slightly with increasing porogen loading. At porogen loadings $\geq$30% (30%–50%), the porous SiC_xN_y films maintained almost constant porosity (at 20.0%) but exhibited an increased pore size at 40%–50% loading, which slightly reduced the mechanical strength (from 7.7 to 5.9 GPa), although the dielectric constant remained nearly the same (3.12–3.18). At this stage, the elastic modulus was determined by both pore size and porosity,[31] whereas the dielectric constant depended mainly on porosity.

When porogen loading was fixed at 20% to ensure that the film did not collapse after thermal treatment at 400°C, the elastic moduli of porous SiC_xN_y films increased from 8.7 to 32.9 GPa when the deposition temperature was increased from 100 to 300°C (Table II). This can be attributed to SiC_xN_y films becoming denser or film porosity

Table II. Pore morphology and properties of porous low-k SiC_xN_y films for various deposition temperatures at 20% ECH loading.

Deposition temperatures (°C)	D (nm)	L (nm)	Porosity (%)	Modulus (GPa)	k
100	3.8 ± 0.2	68.2	12.3	8.7	3.27
150	3.6 ± 0.3	64.3	-	11.9	3.55
200	3.6 ± 0.3	47.0	8.6	15.3	3.73
250	3.2 ± 0.3	41.7	-	28.2	3.98
300	3.0 ± 0.2	-	5.3	32.9	4.13

Downloaded on 2015-03-15 to IP 60.251.210.233 address. Redistribution subject to ECS terms of use (see ecsdl.org/site/terms_use) unless CC License in place (see abstract).

decreasing with increasing deposition temperature, but with pore sizes changing only within a small range, between 3.8 nm (100°C) and 3.0 nm (300°C). Similarly, the dielectric constant of the porous SiC_xN_y films increased from 3.27 to 4.13 with an increase in deposition temperature.

Conclusions

Low-k porous SiC_xN_y films were deposited by performing PECVD, using VSZ as the matrix precursor, and ECH as the porogen; after deposition, films were annealed at 400°C for 3 h to remove the sacrificial porogen. The effects of porogen loading and deposition temperature on porogen incorporation, porosity, pore morphology, and the properties of porous SiC_xN_y films are described in this report. The results revealed that in the as-deposited SiC_xN_y/porogen hybrid films, the porogen/pore size increased slightly relative to the pore size in the SiC_xN_y film (4.9 nm) prepared using pure VSZ (0% ECH) when the ECH loading was increased from 10% to 50%. The ECH porogen and its fragments filled the void in the SiC_xN_y matrix generated from pure VSZ. The amount of incorporated porogen increased linearly, up to 30% porogen loading, after which the incorporation increased at a higher rate with an increase in porogen loading. When a small amount of porogen (<30% ECH loading) was incorporated into the film, the porogens increased the pore correlation distance only slightly, but did not disrupt the short-range ordering in pore arrangement. At ≥30% ECH loadings, the increase in porogen incorporation led to enhanced randomness in porogen distribution in the films.

After annealing the films at 400°C for 3 h, the porosity of the SiC_xN_y films deposited at 100°C increased from 1.8% to 19.8% with increasing porogen loading, up to a threshold ECH loading of 30%, above which the porosity remained nearly constant because of a substantial increase in film shrinkage. The pore size decreased slightly, from 4.1 to 3.7 nm, when ECH loading increased from 0% to 30%, above which larger pore sizes (5.1–5.3 nm) and board pore distributions were observed because of the porogen aggregation and decomposition and the film shrinkage caused by the annealing. Both the elastic modulus and the dielectric constant decreased with increasing porosity. By contrast, under 20% ECH loading, an increase in deposition temperatures led to a decrease in porogen incorporation and film densification. The porosities and pore size of SiC_xN_y films decreased from 12.3% to 5.3% and from 3.8 to 3.0 nm when deposition temperature increased from 100 to 300°C, respectively. The short-range ordering in pore arrangement, exhibiting various pore correlation distances, was observed only at deposition temperature ≤ 250°C because the N-Si-C cross-linked matrix structures and organic phase were present at low temperatures. The elastic moduli and the dielectric constants of porous SiC_xN_y films ranged from 8.7 to 32.9 GPa and from 3.27 to 4.13, respectively. The elastic modulus of the SiC_xN_y film was determined by both pore size and porosity, whereas the dielectric constant depended mainly on porosity. Thus, when introducing porosity into SiC_xN_y films prepared using the PECVD technique, the level of porogen incorporation is determined by porogen loading and its volatility (and hence deposition temperature), as well as by porogen aggregation and film shrinkage during the thermal decomposition step. Using optimal condition, a low-k porous SiC_xN_y film was fabricated in this study, which exhibited a k value of 3.18 and an elastic modulus of 7.7 GPa at 19.8% porosity and 3.7-nm pore size.

Acknowledgments

The authors are grateful for the financial support provided by National Science Council of the ROC, under Contract No. NSC 101-2221-E-009-126-MY2 and MOST 103-2221-E-009-181-MY3. The technical discussion with Dr. Wen-Li Wu of NIST is also appreciated.

References

1. D. Ingerly, A. Agrawal, R. Ascazubi, A. Blattner, M. Buehler, V. Chikarmane, B. Choudhury, F. Cinnor, C. Ege, C. Ganpule, T. Glassman, R. Grover, P. Hentges, J. Hicks, D. Jones, A. Kandas, H. Khan, N. Lazo, K. S. Lee, H. Liu, A. Madhavan, R. McFadden, T. Mule', D. Parsons, P. Parthangal, S. Rangaraj, D. Rao, J. Roesler, A. Schmitz, M. Sharma, J. Shin, Y. Shusterman, N. Speer, P. Tiwari, G. Wang, P. Yashar, and K. Mistry, *Conference Proceedings of the IEEE International Interconnect Technology (IITC)* (2012).
2. S. M. Smith, T. Tighe, D. Convey, J. Quintero, and Y. Wei, *Thin Solid Films*, **516**, 885 (2008).
3. I. Martin, M. Vetter, A. Orpella, C. Voz, J. Puigdollers, and R. Alcubilla, *Appl. Phys. Lett.*, **81**, 4461 (2002).
4. H. Cui and P. A. Burke, *J. Electrochem. Soc.*, **151**(11), G795 (2004).
5. N. Fainer, Y. Rumyantsev, M. Kosinova, E. Maximovski, V. Kesler, V. Kirienko, and F. Kuznetsov, *Surf. Coat. Technol.*, **201**, 9269 (2007).
6. A. Mallikarjunan, A. D. Johnson, L. Matz, R. N. Vrtis, A. Derecskei-Kovacs, X. Jiang, and M. Xiao, *Microelectron. Eng.*, **92**, 83 (2012).
7. S. V. Nguyen, A. Grill, S. Cohen, H. Shobha, N Klymko, E. Simonyi, T. Haigh Jr., C. Hu, E. Adams, E. Linger, A. Madan, T. Shaw, E. T. Ryan, T. Cheng, J. Herman, and R. Young, Abstract No. 2159, the *216th ECS Meeting proceeding*, Vienna, Austria (2009)
8. C. C. Chiang, I. H. Ko, M. C. Chen, Z. C. Wu, Y. C. Lu, S. M. Jang, and M. S. Liang, *J. Electrochem. Soc.*, **151**(2), G93 (2004).
9. T. Ishigami, T. Kurokawa, Y. Kakuhara, B. Withers, J. Jacobs, A. Kolics, I. Ivanov, M. Sekine, and K. Ueno, p, 75, *Proceedings of the IEEE IITC* (2004).
10. I. Kume, M. Ueki, N. Inoue, J. Kawahara, N. Ikarashi, N. Furutake, S. Saitoh, and Y. Hayashi, *Jpn. J. Appl. Phys.*, **50**, 04DB02 (2011).
11. H. E. Tu, Y. H. Chen, and J. Leu, *J. Electrochem. Soc.*, **159**(5), G56 (2012).
12. H. E. Tu, C. J. Su, U. Jeng, and J. Leu, to be published (submitted to *Thin Solid Films* and under review).
13. A. Guinier and G. Fournet, *Small-Angle Scattering of X-rays*, John Wiley & Sons, New York (1955).
14. M. Baklanov, M. Green, and K. Maex, *Dielectric Films for Advanced Microelectronicss*, John Wiley & Sons Ltd, New York (2007).
15. C. H. Hsu, U. S. Jeng, H. Y. Lee, C. M. Huang, K. S. Liang, D. Windover, T. M. Lu, and C. Jin, *Thin Solid Films*, **472**, 323 (2005).
16. W. C. Oliver and G. M. Pharr, *J. Mater. Res.*, **7**, 1564 (1992).
17. R. J. Roe, *Methods of X-Ray and Neutron Scattering in Polymer Science*, Oxford University Press, New York (2000).
18. K. Heo, S. G. Park, J. Yoon, K. S. Jin, S. Jin, S. W. Rhee, and M. Ree, *J. Phys. Chem. C*, **111**, 10848 (2007).
19. S. M. Gates, D. A. Neumayer, M. H. Sherwood, A. Grill, X. Wang, and M. Sankarapandian, *J. Appl. Phys.*, **101**, 094103 (2007).
20. A. Grill and D. A. Neumayer, *J. Appl. Phys.*, **94**, 6697 (2003).
21. L. Favennec, V. Jousseaume, G. Gerbaud, A. Zenasni, and G. Passemard, *J. Appl. Phys.*, **102**, 064107 (2007).
22. M. L. Josien, N. Fuson, J. M. Lebas, and T. M. Gregory, *J. Chem. Phys.*, **21**, 331 (1953).
23. M. Govindarajan, S. Periandy, and K. Ganesan, *E-J. Chem.*, **7**(2), 457 (2010).
24. A. Castex, V. Jousseaume, J. Deval, J. Bruat, L. Favennec, and G. Passemard, *J. Vac. Sci. Technol. A*, **26**(5), 1343 (2008).
25. D. Merche, C. Poleunis, P. Bertrand, M. Sferrazza, and F. Reniers, *IEEE Trans. Plasma Sci.*, **37**, 951 (2009).
26. A. M. Wrobel, I. Blaszczyk-Lezak, A. Walkiewicz-Pietrzykowska, T. Aoki, and J. Kulpinski, *J. Electrochem. Soc.*, **155**(4), K66 (2008).
27. Z. Chen, K. Prasad, C. Y. Li, S. S. Su, D. Gui, P. W. Lu, X. He, and S. Balakumar, *Thin Solid Films*, **462-463**, 223 (2004).
28. Y. Lin, T. Y. Tsui, and J. J. Vlassak, *J. Electrochem. Soc.*, **153**(7), F144 (2006).
29. R.A.B. Devine, *J. Vac. Sci. Technol. A*, **6**, 3154 (1988).
30. H. Imai, K. Awazu, M. Yasumori, H. Onuki, and H. Hirashima, *J. Sol-Gel Sci. Technol.*, **8**, 365 (1997).
31. K. K. Phani and S. K. Niyogi, *J. Mater. Sci.* **22**, 257 (1987).

Downloaded on 2015-03-15 to IP **60.251.210.233** address. Redistribution subject to ECS terms of use (see **ecsdl.org/site/terms_use**) unless CC License in place (see abstract).